CrystEngComm

Accepted Manuscript

ROYAL SOCIETY OF CHEMISTRY

www.rsc.org/crystengcomm

Graphical abstract

for

A plasma-assisted approach for the controlled dispersion of CuO aggregates into β iron(III) oxide matrices.

Giorgio Carraro,[a] Alberto Gasparotto,[a] Chiara Maccato,[a] Elza Bontempi,[b] Fabjola Bilo,[b] Daniel Peeters,[a] Cinzia Sada,[c] and Davide Barreca[d]*

[a] Department of Chemistry, Padova University and INSTM, 35131 Padova, Italy.

[b] Chemistry for Technologies Laboratory, Brescia University and INSTM, 25123 Brescia, Italy.

[c] Department of Physics and Astronomy, Padova University, 35131 Padova, Italy.

[d] CNR-IENI and INSTM, Department of Chemistry, Padova University - 35131 Padova, Italy.

E-mail: davide.barreca@unipd.it

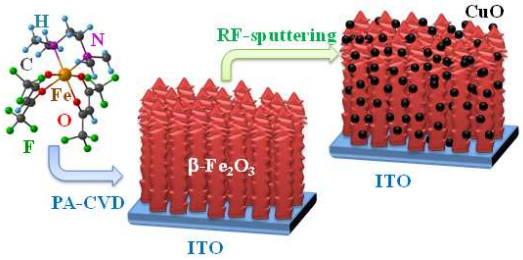

High purity supported β-Fe_2O_3/CuO nanosystems with tailored morphology and tuneable copper content were fabricated by a two-step plasma-assisted process.

Cite this: DOI: 10.1039/c0xx00000x

www.rsc.org/xxxxxx

ARTICLE TYPE

A plasma-assisted approach for the controlled dispersion of CuO aggregates into β iron(III) oxide matrices

Giorgio Carraro,[a] Alberto Gasparotto,[a] Chiara Maccato,[a] Elza Bontempi,[b] Fabjola Bilo,[b] Daniel Peeters,[a] Cinzia Sada,[c] and Davide Barreca*[d]

Received (in XXX, XXX) Xth XXXXXXXXX 20XX, Accepted Xth XXXXXXXXX 20XX
DOI: 10.1039/b000000x

β-Fe_2O_3/CuO nanosystems were synthesised by using a two-step plasma-assisted strategy. β-Fe_2O_3 nanostructures (*host*) were initially deposited by plasma assisted-chemical vapour deposition (PA-CVD) on indium tin oxide (ITO) substrates. Subsequently, CuO nanoparticles (NPs, *guest*) were over-deposited on *host* matrices by means of radio frequency (RF)-sputtering under mild conditions. The combined use of structural, morphological and chemical analyses evidenced the formation of pure and homogeneous β-Fe_2O_3/CuO systems, possessing a high dispersion of CuO NPs in/on β-Fe_2O_3 *hosts*. The target nanomaterials were characterized by an intimate contact between the two oxides, with CuO NPs size and content tuneable as a function of sputtering time. These features, along with the tailored nano-organization, make the present β-Fe_2O_3/CuO nanosystems attractive candidates for diverse technological applications involving solar light harvesting.

1 Introduction

One of most appealing targets in the science and technology of functional oxides is represented by the preparation of multicomponent oxide nanosystems.[1-7] In this widespread scenario, the surface modification of metal oxide matrices with suitable functional activators is an attractive strategy to develop *host-guest* composites with an intimate contact between constituents, attaining a favourable interplay between their chemical and electronic properties.[8-15]

In this context, an attractive option involves the fabrication of composite nanostructures based on the combination of *p*- and *n*-type semiconducting oxides.[16-20] The enhanced functional performances of these systems with respect to their single-phase counterparts can be mainly traced back to the formation of an inner electric field at the *p*-*n* junction interface.[18,21] This phenomenon, in turn, can be considered responsible for an improved separation of electron–hole pairs, with positive impact on eventual applications in optoelectronics, gas sensing and photocatalysis (pollutant degradation, H_2 generation,…).[12,19,20,22] Among oxide composites, systems based on Fe_2O_3, an *n*-type semiconductor, have drawn an increasing attention for various end-uses, such as (photo)catalysis, Li-ion batteries, molecular detection and magnetic devices.[8,10,13,14,23-27] Beyond the most thermodynamically stable α-Fe_2O_3 (*hematite*), other scarcely occurring iron(III) oxide polymorphs, such as β-Fe_2O_3 (*bixbyite*), have recently come under study for the possible birth of novel functional properties.[28-30] Nevertheless, up to date, reports of β-Fe_2O_3-based nanocomposites are scarce and this issue undoubtedly deserved further attention.

Recently, we have focused our attention on the development of metal-containing β-Fe_2O_3 nanosystems.[23] The target materials, synthesized by chemical vapour deposition (CVD) of iron(III) oxide, followed by radio frequency (RF)-sputtering of Ag or Pt nanoparticles (NPs), have been shown to possess an improved gas sensing behaviour with respect to bare β-Fe_2O_3, thanks to the sensitizing action of the introduced NPs. An alternative approach to tune the resulting material properties involves the dispersion of a second oxide as a possible substitute for more expensive/toxic metals (such as Ni, Pd or Pt).[14,26] In this regard, CuO, a *p*-type semiconductor, is an appealing candidate thanks to its chemical reactivity, that has fuelled its use in various composites for gas sensing, wastewater treatment, and green energy generation.[3,8,21,31,32] In addition, the capability of capturing a certain fraction of the solar spectrum renders CuO an attractive candidate for use in photo-assisted hydrogen production.[3] Recently, we have successfully developed ZnO-based nanocomposites involving the introduction of CuO as a functional activator to improve the system behaviour in H_2 production by direct photocatalysis, as well as in the highly efficient sensing for various analytes.[16,17] Basing on these data, the fabrication of β-Fe_2O_3/CuO nanomaterials is an attractive challenge from both a fundamental and an applicative point of view.

In this context, the development of β-Fe_2O_3/CuO nanocomposites with a controlled composition/morphology and a tuneable component distribution is a key issue to master performances by exploiting the synergistic constituent chemical interactions at their interface.[9,16]

This work presents a fundamental study on supported β-Fe_2O_3/CuO nanocomposites obtained by a full plasma-assisted strategy. The utility and flexibility of cold plasmas used for the above routes are due to their high chemical reactivity even in the

absence of external thermal supplies, enabling material processing at temperatures lower than conventional vapor-phase routes. As a consequence, PA-CVD processes can be considered more cost-effective than the homologous thermal CVD ones. Similar observations hold even for Radio Frequency (RF)-sputtering processes,[33] used in the present work for the functionalization of Fe_2O_3 matrices with CuO species.

As exemplified in Scheme 1, the adopted synthetic route is based on the initial plasma assisted (PA)-CVD of single-phase β-Fe_2O_3, followed by RF-sputtering of Cu from Ar plasmas under mild conditions, in order to avoid undesired alterations of the pristine iron(III) *host* matrices.[2,16,17] The processing parameters were optimized in order to ensure the dispersion of CuO particles into Fe_2O_3, avoiding the formation of continuous films. Finally, *ex-situ* thermal treatments in air were carried out in order to stabilize the obtained composites, ensuring a quantitative copper oxidation to CuO. Key advantages of the proposed approach are the possibility of achieving a tailored in-depth dispersion of CuO NPs into β-Fe_2O_3 *host* matrices, as well as the capability of modulating both CuO NPs content and size by variations of the sole sputtering time. A multi-technique characterization was carried out to elucidate the interplay between nanocomposite features and synthesis conditions, with particular attention to copper content and chemical state. Morphological and optical properties were also investigated in view of possible technological utilizations of the developed materials.

2 Experimental

2.1. Synthesis

Fe_2O_3 matrices were fabricated by means of a custom-built plasma assisted-chemical vapour deposition (PA-CVD) apparatus equipped with a RF generator (Cesar 133, Thin Films, Padova, Italy; ν = 13.56 MHz),[28,34] consisting of a vacuum metal chamber with two vertical and parallel electrodes (diameter = 90 mm). RF power was delivered to one of the electrodes through a coaxial cable connected to a matching box (VM 1000, Thin Films, Padova, Italy). The substrates were mounted on a second electrode, electrically connected with the chamber walls (grounded), whose temperature was measured by a thermocouple inserted into a resistively heated sample holder.

Growth experiments were performed from electronic grade Ar/O_2 plasmas at 10 W RF-power (duration = 1 h), operating at a total pressure of 1.0 mbar, with a fixed inter-electrode distance was fixed at 60 mm. The iron precursor $Fe(hfa)_2TMEDA$ (hfa = 1,1,1,5,5,5 - hexafluoro - 2,4 - pentanedionate; TMEDA = *N*,*N*,*N'*,*N'* - tetramethylethylenediamine), synthesized according to a previously reported procedure,[35,36] was placed in an external glass reservoir, heated by an oil bath at 65°C, and transported into the reaction chamber by an Ar flow (rate = 60 sccm). The temperature of precursor feeding lines was maintained at 140°C through heating tapes, to prevent detrimental condensation phenomena. Two further auxiliary gas-lines were used to introduce Ar (rate = 15 sccm) and O_2 (rate = 20 sccm) directly into the reactor chamber. Fe_2O_3 growth was performed at 400°C on indium tin oxide (ITO)-coated borosilicate substrates (Präzisions Glas & Optik GmbH, CEC010B, 10 Ω/sq; ITO thickness ≈ 200 nm, size = 20 mm × 10 mm × 1.1 mm). The choice of the substrate was performed in view of eventual applications in photo-assisted processes, such as photoeletrochemical water splitting.[28] Prior to deposition, the substrates were suitably cleaned by iterative dipping in an aqueous solution of sulphonic detergent, distilled water, acetone, and isopropyl alcohol, and finally dried under an Ar flow.

Subsequently, copper deposition on iron(III) oxide *hosts* was performed by RF-sputtering through the above described instrumental apparatus, using Ar as plasma source. A copper target (Alfa Aesar®; thickness = 0.3 mm; purity = 99.95 %) was fixed on the RF electrode, whereas ITO-supported Fe_2O_3 specimens were placed on the ground electrode. After degassing the chamber to $<10^{-5}$ mbar in order to minimize the presence of atmospheric residuals, sputtering processes were carried out under the following optimized conditions: substrate temperature = 60°C; RF-power = 5 W; total pressure = 0.3 mbar; Ar flow rate = 10 sccm; electrode-to-electrode distance = 50 mm; experiment duration = 1, 2 or 3 h. These parameters were chosen so as to tailor the overall copper content and ensure, at the same time, a moderate Cu content, avoiding the complete coverage of the underlying Fe_2O_3 matrices. The resulting composites were subjected to *ex-situ* thermal treatments in air at 400°C for 1 h to attain a complete copper oxidation and material stabilization.

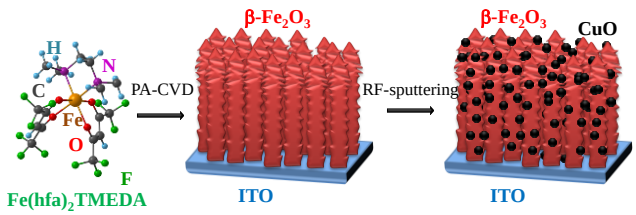

Scheme 1 Sketch of the synthetic route adopted for Fe_2O_3/CuO nanocomposites.

2.2. Characterization

2D X-ray microdiffraction (XRD^2) measurements were run in reflection mode (acquisition time = 30 min) on a Dymax-RAPID X-ray microdiffractometer, with a cylindrical imaging plate detector, that allows collecting from 0 to 160° (2ϑ) horizontally and from –45 to +45° (2ϑ) vertically upon using CuKα radiation. A collimator diameter of 300 μm was used. Conventional XRD patterns were then obtained by integration of 2D images.

Plane-view (pv) and cross-sectional (cs) field emission-scanning electron microscopy (FE-SEM) micrographs were collected by a Zeiss SUPRA 40VP field emission instrument, at a primary beam voltage of 10.0 kV. The mean nanostructure length was evaluated basing on cross-sectional images, by averaging over 20 independent measurements for each specimen.

Line-scan EDXS analyses were carried out by monitoring the FeKα, OKα and CuKα signals throughout the deposit thickness by an Oxford INCA x-sight X-ray detector (primary beam acceleration voltage = 20.0 kV).

Surface X-ray photoelectron spectroscopy (XPS) measurements were performed on a Perkin-Elmer Φ 5600ci spectrometer using a standard MgKα radiation (energy = 1253.6 eV), at a working pressure lower than 10^{-8} mbar. The reported binding energies (BEs, standard deviation = ± 0.2 eV) were corrected for charging by assigning to the adventitious C1s signal a BE of 284.8 eV. The

analysis involved Shirley-type background subtraction and, whenever necessary, spectral decomposition by fitting with Gaussian–Lorentzian functions.[37] Atomic percentages (at.%) were calculated by peak integration using standard PHI V5.4A sensitivity factors.

Total reflection X-ray (TXRF) measurements were collected by a GNR Explorer diffractometer equipped with a Si drift energy dispersive detector to collect fluorescence spectra in total reflection mode.[38] Samples were aligned following standard procedures for X-ray reflectivity measurements with the aid of a NaI(Tl) scintillation detector.

In-depth secondary ion mass spectrometry (SIMS) analyses were carried out by means of an IMS 4f mass spectrometer (Cameca) using a 14.5 KeV Cs^+ primary beam (current = 25 nA, stability = 0.3%) and by negative secondary ion detection, using an electron gun for charge compensation. Beam blanking mode and high mass resolution configuration were adopted. Signals were recorded rastering over a 175 × 175 μm^2 area and detecting secondary ions from a sub-region close to 10 × 10 μm^2 to avoid crater effects.

UV-Vis-NIR optical absorption spectra were recorded in transmission mode at normal incidence by means of a Cary 5E dual-beam spectrometer, subtracting the ITO substrate contribution. Optical penetration depth values (α^{-1}, where α is the absorption coefficient) were calculated by the following relation:[27,28,39]

$$\alpha^{-1} = -D \times [\ln(T)]^{-1} \quad (1)$$

where D is the overall deposit thickness determined by cross-sectional FE-SEM images and T is the measured transmittance.

3 Results and discussions

In order to attain an insight into the system microstructure, with particular attention to the possible co-presence of different Fe_2O_3 polymorphs or to the formation of Fe-Cu-O ternary phases, the phase composition is investigated by XRD[2] analyses (Fig. 1). In particular, peaks at 23.1°, 32.9°, 38.1° and 40.7° can be assigned to (211), (222), (400) and (411) reflections of cubic β-Fe_2O_3[40] and no signals from other iron(III) oxide polymorphs are clearly detected. In addition, due to relatively high X-ray penetration depth, even the substrate signals are detected.[41] As already reported for iron(III) oxide systems deposited by PA-CVD, the formation of the β phase can be traced back to the fact that the ITO substrate possesses very similar lattice parameters to those of the present Fe_2O_3 polymorph.[28,40,41] Remarkably, no reflections related to Cu-containing species are detectable, suggesting a high copper dispersion even for a sputtering time of 3 h. In addition, no signals related to Fe-Cu-O ternary phases are present, confirming that the adopted synthesis conditions are mild enough to preserve the initial β-Fe_2O_3 identity.

To investigate the system nano-organization, both plane-view and cross-sectional FE-SEM images of Fe_2O_3/CuO nanocomposites were recorded (Fig. 2). In general, the composite morphology is reminiscent of the bare iron oxide matrix [compare Fig. S1, Electronic Supplementary Information (ESI)†], being characterized by homogeneously distributed nanoplatelet arrays grown perpendicular to the ITO substrate surface. Cross-sectional images suggest an appreciable system porosity, as demonstrated by the occurrence of voids between β-Fe_2O_3 structures (mean length = 370±20 nm). Interestingly, the presence of iron(III) oxide nanoplatelets with reduced lateral size can result in an enhanced light harvesting, along with a short charge carrier

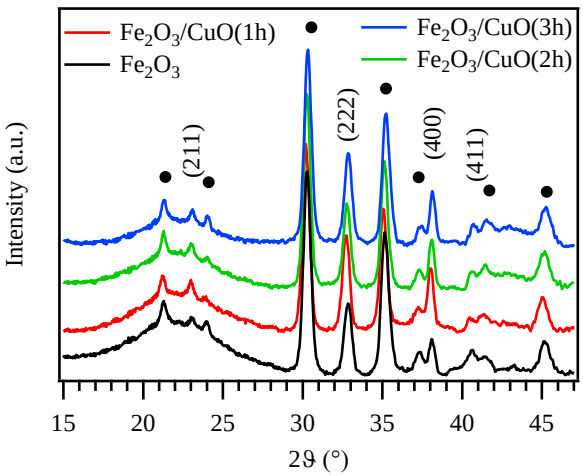

Fig. 1 XRD[2] integrated patterns of pure β-Fe_2O_3 and β-Fe_2O_3/CuO nanocomposites prepared adopting various copper sputtering times. Reflections attributed to the ITO substrate are marked with (•).

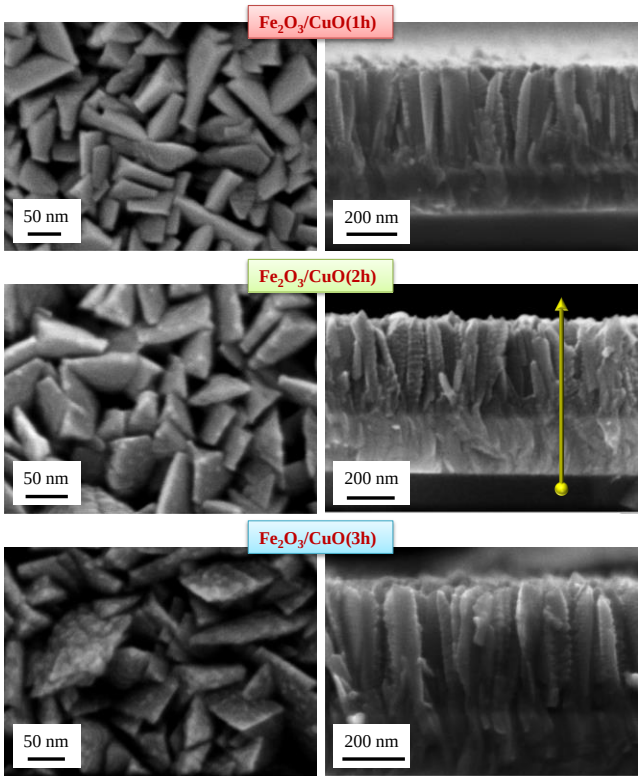

Fig. 2 Pv and cs FE-SEM micrographs of Fe_2O_3/CuO nanocomposites prepared at various copper sputtering times.

transport distance, minimizing thus detrimental recombination losses.[42,43] In addition, the high active area of such systems suggests an efficient dispersion of the *guest* phase into the *host* matrix. To this regard, as shown by pv SEM images (Fig. 2), iron(III) oxide structures are decorated by a dispersion of Cu-containing aggregates, whose density and average sizes increase with the corresponding sputtering time.

After 1 h of Cu sputtering, small and sparsely distributed aggregates are detected, whereas the occurrence of closer NPs is observed upon increasing the sputtering time up to 2 and 3 h. Correspondingly, the average particle size increases from 10±2 to 14±2 nm. As a matter of fact, this NP size increase could be ascribed to a progressive increase of the sputtered CuO amount and, in particular, to the preferential interaction of impinging particles with preformed copper(II) oxide nucleation sites rather than with Fe_2O_3, according to a three-dimensional (3D) growth mechanism.

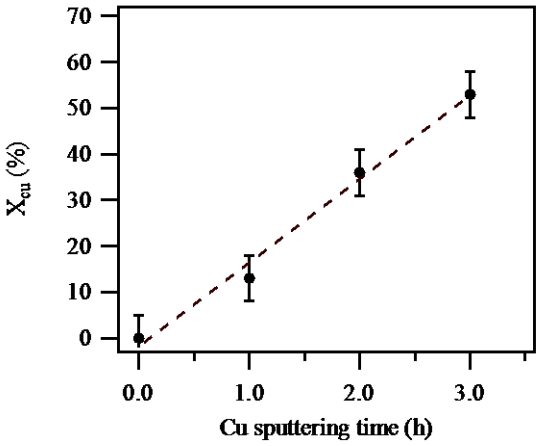

Fig. 3 Surface X_{Cu} as a function of the adopted copper sputtering time.

The surface chemical composition of Fe_2O_3/CuO nanocomposites was analysed by XPS. The disappearance of carbon peaks to noise level after 10 min of Ar^+ erosion confirms the system purity. The analysis of the O1s peak (not reported) reveals the presence of a main component located at 530.0 eV, attributed to lattice O in iron(III) and copper(II) oxides, with a tailing at 531.8 eV due to surface chemisorbed hydroxyl/carbonate species.[23,28,44-46] The $Fe2p_{3/2}$ position (BE = 710.9 eV, see Fig. S2a, ESI†) is in good agreement with the presence of Fe(III) in Fe_2O_3.[23,26,44-46] The Cu2p band (Fig. S2b, ESI†) is characterized by intense *shake-up* satellites located 8.6 eV higher than the main *spin-orbit* components [BE($Cu2p_{3/2}$) = 934.3 eV; BE($Cu2p_{1/2}$) = 954.0 eV]. These spectral features, along with the copper Auger parameter [α = KE(CuL_3MM) + (BE($Cu2p_{3/2}$) = 1851.4 eV], confirm the occurrence of Cu(II) oxide as the predominant copper species in all samples.[16,17,21,37,44,46] The surface copper molar fraction [X_{Cu} = Cu at.% / (Cu at.% + Fe at.%) × 100] calculated from XPS analyses (Fig. 3) displays a linear increase with sputtering time, as already observed for M-oxide nanocomposites (M = metal/oxide) obtained by M sputtering onto suitable substrates.[17,47]

In order to establish whether this linear trend was valid only for the system outermost layers, sampled by XPS, or for the overall specimens, TXRF analyses were undertaken. TXRF patterns collected on Fe_2O_3/CuO nanocomposites (Fig. 4a) show the signals related to FeKα, FeKβ and CuKα. The main contribution with almost the same intensity in all spectra is due to Fe peaks, whereas a weaker signal at ≈ 8 keV can be attributed to CuKα emission, with an intensity proportional to the copper sputtering time. The relative Cu content, calculated with respect to Fe amount, was 1, 2 and 3 % after sputtering times of 1 h, 2 h and 3 h.

To get further information on the local in-depth Fe_2O_3/CuO composition, EDXS line-scan analyses are carried out, and representative data are proposed in Fig 4b.

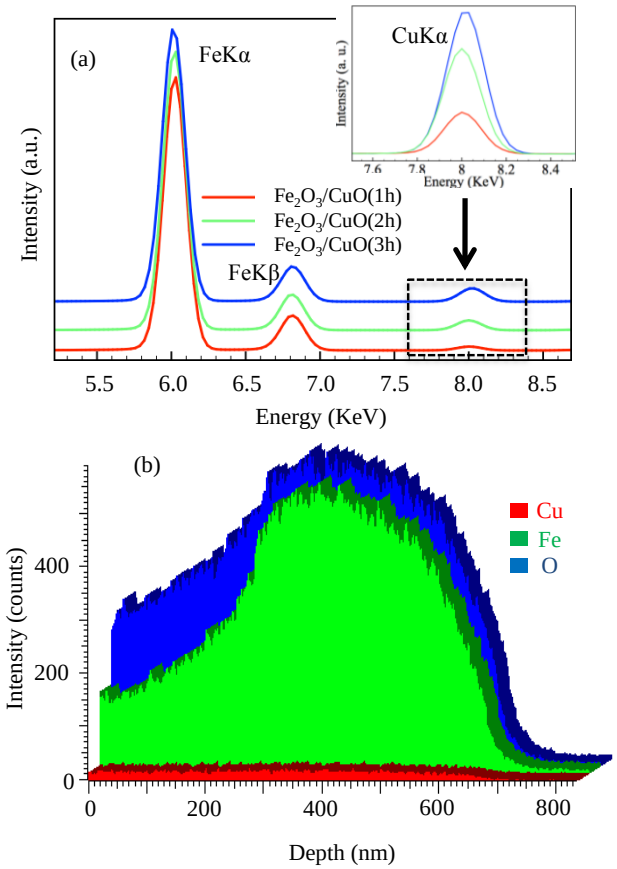

Fig. 4 (a) TXRF patterns collected on Fe_2O_3/CuO samples. Spectra are vertically shifted for clarify. A magnification of the CuKα region is reported in the inset. (b) Representative EDXS scans along the line marked in Fig. 2 for Fe_2O_3/CuO(2h). The red, green, and blue traces correspond to CuKα1, FeKα1, and OKα1 X-ray signals, respectively.

The results evidence a parallel trend of O and Fe signals, suggesting a common chemical origin for the two species, as expected for Fe_2O_3 materials. It is worth noticing that a uniform copper distribution throughout the entire deposit thickness is obtained. In order to further investigate the system composition, with particular attention to the copper spatial distribution, SIMS depth profiles are carried out on Fe_2O_3/CuO nanocomposites (Fig. 5). In general, all samples present homogeneous Fe, O and Cu profiles, pointing out to a uniform chemical composition throughout the nanodeposit thickness. As can be noticed, both copper and iron signals undergo a drop-off upon to the increase of the In signal, evidencing a sharp interface with the ITO substrate. Irrespective of the processing conditions, the O ionic yield remained almost constant throughout the deposit thickness.

In order to investigate the light harvesting properties of the present Fe_2O_3/CuO nanocomposites, UV-Vis-NIR absorption spectra are recorded (Fig. 6). In all cases, the spectral shape is in good agreement with the one for β-Fe_2O_3 data polymorph, exhibiting a prominent absorption in the Vis region for λ < 700 nm, related to interband transitions.[28,35]

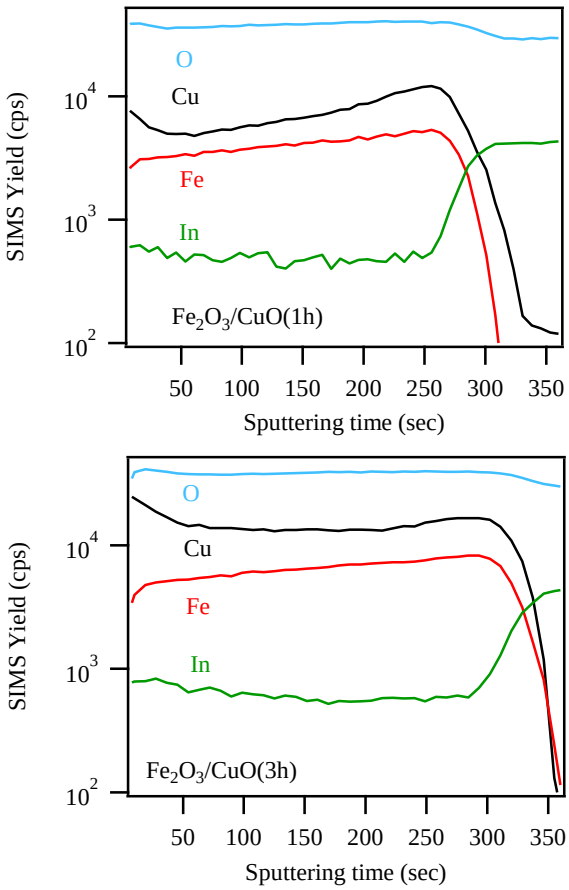

Fig. 5 SIMS depth profiles for Fe_2O_3/CuO nanocomposites obtained with a copper sputtering time of 1 h and 3 h.

The dispersion of CuO NPs in the iron(III) oxide matrices produces an increased light absorption with respect to the pure Fe_2O_3 system. In particular, the optical penetration depth (α^{-1}) at λ = 470 nm decreases from 150 to 120 nm upon going from the bare matrix to the composite with the highest CuO loading (sputtering time = 3 h). Considering that α^{-1} corresponds to the distance over which 63% of photons are absorbed,[28] these data suggest that CuO introduction promotes light harvesting in the outermost material region. From the optical absorption spectra, band gap energies (E_G) are evaluated by plotting $(\alpha h\nu)^2$ as a function of photon energy $h\nu$ (Tauc plots, Fig. 6a).[28,39] As can be observed, no significant E_G variations occurred upon CuO introduction. A detailed analysis of β-Fe_2O_3 optical spectra with different nanodeposits thickness revealed the appearance of a weak band in the 620-750 nm range, whose exact position depends on the system thickness, similarly to the present case (compare Fig. 6). Such a phenomenon, that could be related to interference fringes, precludes a detailed attribution of the above band to the presence of CuO (E_G = 1.2 eV), which would give rise to an absorption in the same spectral range.[48-50]

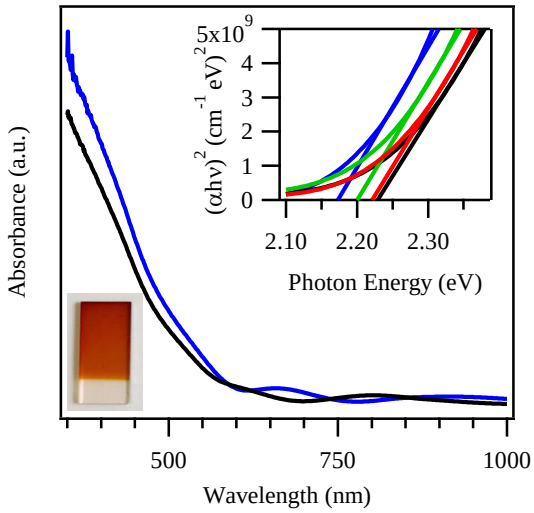

Fig. 6 Optical absorption spectra and Tauc plots (inset) obtained with n = 2 for Fe_2O_3/CuO samples. Colour codes: black, pure Fe_2O_3; red, Fe_2O_3/CuO(1h); green, Fe_2O_3/CuO(2h); blue, Fe_2O_3/CuO(3h). The image on the bottom left represents a representative photograph of a Fe_2O_3/CuO nanocomposites.

Conclusions

In summary, the present work has reported on a plasma-assisted strategy for the fabrication of supported β-Fe_2O_3/CuO nanocomposites. The target materials have been developed and tailored by a two-step PA-CVD/RF-sputtering approach, with attention to the influence of Cu sputtering time on the system characteristics. The obtainment of β-Fe_2O_3 nanoplatelet arrays with an inherent porosity, along with the infiltration power characterizing RF-sputtering, has enabled to develop high purity Fe_2O_3/CuO nanocomposites. These systems were characterized by the presence of the sole β-Fe_2O_3 polymorph and presented an uniform distribution of CuO NPs. Controlled variations of the sole sputtering time enabled to tailor both the size and amount of copper(II) oxide nanoaggregates. Furthermore, optical spectroscopy studies suggested that CuO introduction might favour an improved radiation absorption in the Vis range, of importance for applications requiring solar light harvesting. Future perspectives for further developments of the present work will involve high-resolution transmission electron microscopy (TEM) observations, to shed further light into the CuO/β-Fe_2O_3 interface and the local nano-scale investigation of the system structure. Additional exploitation of the presented PA-CVD/sputtering approach can also disclose interesting perspectives for the fabrication of other binary/ternary composites, such as Fe_2O_3/WO_3 activated by Ag/Au NPs. These materials may have other intriguing applications in a variety of end-uses, encompassing highly efficient sensors, energy storage and optoelectronics.

Acknowledgements

The research leading to these results has received funding from the European Community's Seventh Framework Program (FP7/2007-2013) under grant agreement No. ENHANCE-238409. The authors also kindly acknowledge the financial

support under the FP7 project "SOLAROGENIX" (NMP4-SL-2012-310333), as well as from Padova University ex-60% 2012-2013 projects, Padova University SOLLEONE (CPDR132937/13), PRAT 2010 (n° CPDA102579) and Regione Lombardia-INSTM ATLANTE projects.

† Electronic Supplementary Information (ESI) available: FE-SEM images for pure β-Fe_2O_3 (Fig. S1); surface XPS Fe2p and Cu2p surface peaks for Fe_2O_3/CuO nanocomposites (Fig. S2).

Notes and references

[a] *Department of Chemistry, Padova University and INSTM, 35131 Padova, Italy.*
[b] *Chemistry for Technologies Laboratory, Brescia University and INSTM, 25123 Brescia, Italy.*
[c] *Department of Physics and Astronomy, Padova University, 35131 Padova, Italy.*
[d] *CNR-IENI and INSTM, Department of Chemistry, Padova University - 35131 Padova, Italy. E-mail: davide.barreca@unipd.it*

1. D. Bekermann, D. Barreca, A. Gasparotto and C. Maccato, *CrystEngComm*, 2012, **14**, 6347-6358.
2. C. Maccato, D. Barreca, G. Carraro, A. Gasparotto, V. Gombac and P. Fornasiero, *Surf. Coat. Technol.*, 2013, **230**, 219-227.
3. D. Barreca, G. Carraro, V. Gombac, A. Gasparotto, C. Maccato, P. Fornasiero and E. Tondello, *Adv. Funct. Mater.*, 2011, **21**, 2611-2623.
4. M. E. A. Warwick, C. W. Dunnill and R. Binions, *Chem. Vap. Dep.*, 2010, **16**, 220-224.
5. A. Paracchino, V. Laporte, K. Sivula, M. Grätzel and E. Thimsen, *Nat. Mater.*, 2011, **10**, 456-461.
6. Q. Zhang, J. Su, X. Zhang, J. Li, A. Zhang and Y. Gao, *New J. Chem.*, 2012, **36**, 2302-2307.
7. X. Jiang, X. Yang, Y. Zhu, K. Fan, P. Zhao and C. Li, *New J. Chem.*, 2013, **37**, 3671-3678.
8. L. Pan, J. Tang and F. Wang, *Central Eur. J. Chem.*, 2013, **11**, 763-773.
9. D. Barreca, A. Gasparotto and E. Tondello, *J. Mat. Chem.*, 2011, **21**, 1648-1654.
10. D. Barreca, G. Carraro, A. Gasparotto, C. Maccato, F. Rossi, G. Salviati, M. Tallarida, C. Das, F. Fresno, D. Korte, U. L. Štangar, M. Franko and D. Schmeisser, *ACS Appl. Mater. Interf.*, 2013, **5**, 7130-7138.
11. N. Bahlawane, K. Kohse-Höinghaus, T. Weimann, P. Hinze, S. Röhe and M. Bäumer, *Ang. Chem. Int. Ed.*, 2011, **50**, 9957-9960.
12. K.-S. Ahn, Y. Yan, M.-S. Kang, J.-Y. Kim, S. Shet, H. Wang, J. Turner and M. Al-Jassim, *Appl. Phys. Lett.*, 2009, **95**, 022116.
13. Y. Kang, L. Wang, Y. Wang, H. Zhang, Y. Wang, D. Hong, Y. Qv and S. Wang, *Sens. Actuators B*, 2013, **177**, 570-576.
14. T. Cheng, Z. Fang, Q. Hu, K. Han, X. Yang and Y. Zhang, *Catal. Comm.*, 2007, **8**, 1167-1171.
15. J. K. Sahoo, M. N. Tahir, M. I. Shukoor, T. D. Schladt, F. Natalio, E. Mugnaioli, U. Kolb and W. Tremel, *New J. Chem.*, 2014, DOI: 10.1039/C1033NJ00989K.
16. Q. Simon, D. Barreca, A. Gasparotto, C. Maccato, T. Montini, V. Gombac, P. Fornasiero, O. I. Lebedev, S. Turner and G. Van Tendeloo, *J. Mater. Chem.*, 2012, **22**, 11739-11747.
17. Q. Simon, D. Barreca, A. Gasparotto, C. Maccato, E. Tondello, C. Sada, E. Comini, G. Sberveglieri, M. Banerjee, K. Xu, A. Devi and R. A. Fischer, *ChemPhysChem*, 2012, **13**, 2342-2348.
18. Y.-F. Wang, M.-C. Hsieh, J.-F. Lee and C.-M. Yang, *Appl. Catal. B*, 2013, **142–143**, 626-632.
19. S.-W. Choi, A. Katoch, J. Zhang and S. S. Kim, *Sens. Actuators B*, 2013, **176**, 585-591.
20. C.-Y. Lin, Y.-H. Lai, D. Mersch and E. Reisner, *Chem. Sci.*, 2012, **3**, 3482-3487.
21. D. Barreca, G. Carraro, E. Comini, A. Gasparotto, C. Maccato, C. Sada, G. Sberveglieri and E. Tondello, *J. Phys. Chem. C*, 2011, **115**, 10510-10517.
22. M. A. Abbasi, Z. H. Ibupoto, A. Khan, O. Nur and M. Willander, *Mater. Lett.*, 2013, **108**, 149-152.
23. G. Carraro, D. Barreca, E. Comini, A. Gasparotto, C. Maccato, C. Sada and G. Sberveglieri, *CrystEngComm*, 2012, **14**, 6469-6476.
24. R. D. Desautels, Y.-Y. Chen, H. Ouyang, S.-C. Lo, J. W. Freeland and J. van Lierop, *J. Appl. Phys.*, 2012, **111**, 07B518.
25. E. García-Tamayo, M. Valvo, U. Lafont, C. Locati, D. Munao and E. M. Kelder, *J. Power Sources*, 2011, **196**, 6425-6432.
26. J.-L. Cao, Y. Wang, X.-L. Yu, S.-R. Wang, S.-H. Wu and Z.-Y. Yuan, *Appl. Catal. B*, 2008, **79**, 26-34.
27. N. T. Hahn and C. B. Mullins, *Chem. Mater.*, 2010, **22**, 6474-6482.
28. D. Barreca, G. Carraro, A. Gasparotto, C. Maccato, C. Sada, A. P. Singh, S. Mathur, A. Mettenbörger, E. Bontempi and L. E. Depero, *Int. J. Hydrogen Energy*, 2013, **38**, 14189-14199.
29. G. Carraro, D. Barreca, C. Maccato, E. Bontempi, L. E. Depero, C. de Julian Fernandez and A. Caneschi, *CrystEngComm*, 2013, **15**, 1039-1042.
30. G. Carraro, C. Maccato, A. Gasparotto, T. Montini, S. Turner, O. I. Lebedev, V. Gombac, G. Adami, G. Van Tendeloo, D. Barreca and P. Fornasiero, *Adv. Funct. Mater.*, 2014, **24**, 372.
31. D. Barreca, P. Fornasiero, A. Gasparotto, V. Gombac, C. Maccato, T. Montini and E. Tondello, *ChemSusChem*, 2009, **2**, 230-233.
32. X.-M. Liu, W.-D. Yin, S.-B. Miao and B.-M. Ji, *Mater. Chem. Phys.*, 2009, **113**, 518-522.
33. A. Gasparotto, D. Barreca, D. Bekermann, A. Devi, R. A. Fischer, C. Maccato and E. Tondello, *J. Nanosci. Nanotechnol.*, 2011, **11**, 8206-8213.
34. D. Barreca, A. Gasparotto, E. Tondello, C. Sada, S. Polizzi and A. Benedetti, *Chem. Vap. Dep.*, 2003, **9**, 199-206.
35. D. Barreca, G. Carraro, A. Devi, E. Fois, A. Gasparotto, R. Seraglia, C. Maccato, C. Sada, G. Tabacchi, E. Tondello, A. Venzo and M. Winter, *Dalton Trans.*, 2012, **41**, 149-155.
36. D. Barreca, G. Carraro, A. Gasparotto, C. Maccato, R. Seraglia and G. Tabacchi, *Inorg. Chim. Acta*, 2012, **380**, 161-166.

37. D. Briggs and M. P. Seah, *Practical surface analysis: Auger and X-ray photoelectron spectroscopy*, John Wiley & Sons: New York, 2nd ed., 1990.
38. L. Borgese, M. Salmistraro, A. Gianoncelli, A. Zacco, R. Lucchini, N. Zimmerman, L. Pisani, G. Siviero, L. E. Depero and E. Bontempi, *Talanta*, 2012, **89**, 99-104.
39. I. Cesar, K. Sivula, A. Kay, R. Zboril and M. Grätzel, *J Phys Chem C*, 2009, **113**, 772-782.
40. *Pattern N°039-0238, JCPDS (2000)*.
41. *Pattern N°01-088-0773 JCPDS (2000)*.
42. A. A. Tahir, K. G. U. Wijayantha, S. Saremi-Yarahmadi, M. Mazhar and V. McKee, *Chem. Mater.*, 2009, **21**, 3763-3772.
43. V. A. N. de Carvalho, R. A. d. S. Luz, B. H. Lima, F. N. Crespilho, E. R. Leite and F. L. Souza, *J. Power Sources*, 2012, **205**, 525-529.
44. J. F. Moulder, W. F. Stickle, P. E. Sobol and K. D. Bomben, *Handbook of X-ray photoelectron spectroscopy*, Perkin Elmer Corporation, Eden Prairie, MN, 1992.
45. G. Carraro, D. Barreca, A. Gasparotto and C. Maccato, *Surf. Sci. Spectra*, 2012, **19**, 1-12.
46. G. Carraro, A. Gasparotto, C. Maccato, D. Peeters and D. Barreca, *Surf. Sci. Spectra*, 2014, **21**, 1-9.
47. L. Armelao, D. Barreca, A. Gasparotto, E. Pierangelo, E. Tondello and S. Polizzi, *J. Nanosci. Nanotechnol.*, 2005, **5**, 259-265.
48. X. Liu, Z. Li, Q. Zhang, F. Li and T. Kong, *Mater. Lett.*, 2012, **72**, 49-52.
49. A. Shui, W. Zhu, L. Xu, D. Qin and Y. Wang, *Ceram. Inter.*, 2013, **39**, 8715-8722.
50. J. Xia, H. Li, Z. Luo, H. Shi, K. Wang, H. Shu and Y. Yan, *J. Phys. Chem. Sol.*, 2009, **70**, 1461-1464.